Systems & Control Transactions

Original Research Article
Peer Reviewed Conference Proceeding
ESCAPE 36 - European Symposium on Computer Aided Process Engineering
Sheffield, UK. 21-24 June 2026

PSE PRESS

Machine Learning-Assisted Multi-PAT Data Fusion for Physics Consistent Crystallization Monitoring

Yiming Ma[a], Xuming Yuan[a], and Brahim Benyahia[a]*

[a] Department of Chemical Engineering, Loughborough University, Leicestershire, LE113TU, United Kingdom
* Corresponding Author: B.Benyahia@lboro.ac.uk.

ABSTRACT

Reliable multimodal monitoring in crystallization processes remains challenging due to heterogeneous PAT signal quality, sensor drift, asynchronous sampling and nonstationary noise. This work presents a machine-learning-assisted fusion framework that integrates multimodal PAT alignment, estimation and physics-guided regularisation to generate coherent concentration and particle-size trajectories. A mechanistically informed simulation platform is developed to produce synthetic Raman, FTIR, FBRM and image-based crystal size data with realistically simulated drift, heteroscedastic noise, dropouts and distortion patterns. Sensor reliability is inferred through a Random Forest model trained on variance-normalised discrepancies and quality metrics, which allows the dynamic adjustment of channel contributions. Across modalities, the Random Forest achieves MAE values of 0.03-0.20 for probability-type indicators and shows stable explanatory power for variance-inflation factors on particle-size channels (R^2 = 0.81-0.93). Two representative PAT scenarios illustrate the performance of the proposed framework under different cross-sensor discrepancy structures, demonstrating improved robustness, reduced local variance and enhanced physical coherence compared with individual signals. Overall, the results highlight the potential of multimodal information fusion as a foundation for trustworthy online monitoring and modelling in crystallization.

Keywords: Machine Learning, Process Monitoring, Modelling and Simulations, Surrogate Model

1. INTRODUCTION

With the rapid progression of continuous manufacturing, digital twins and process intensification, achieving reliable online observability has become central to ensuring product quality and supporting high-fidelity process modeling [1-4]. This need is particularly acute in crystallization-centered systems, where the time dependent evolution of solute concentration and crystal size governs supersaturation control, population-balance dynamics and critical quality attributes [5, 6]. Accurate and high-resolution online measurements that capture the underlying physicochemical evolution are therefore essential for model development, and model-based optimization [7, 8].

Industrial crystallization is typically monitored using process analytical technology (PAT) tools such as Raman and FTIR spectroscopy for concentration estimation, and FBRM or in situ imaging for particle size characterization [9-11]. Although these sensors provide complementary information, their performance in practice is affected by temperature- and solids-dependent spectral drift [12, 13], the structural mismatch between chord length and true particle sizes [14, 15], and imaging artefacts such as defocus or occlusion [16]. Additional challenges arise from asynchronous sampling between fast and slow PAT instruments, which leads to temporal misalignment and apparent discontinuities [17]. While various single sensor enhancement strategies have been proposed, inconsistencies between PAT channels remain common when individual sensors experience degradation or temporary downtime, complicating unified trajectory reconstruction for kinetic modeling, PBM simulation and soft sensing [18, 19].

To obtain more robust estimates of concentration and particle size in particulate processes, researchers have explored signal level fusion strategies, including basic weighting schemes such as inverse-variance

weighting [14, 20], rule-based gating heuristics [21, 22], and classical filtering or smoothing [23, 24] to combine information from heterogeneous PAT channels. While these approaches improve interpretability under relatively stable conditions, their performance remains largely confined to laboratory settings, with limited consideration of realistic industrial signal situations. In response, researchers have increasingly moved towards model level fusion frameworks that explicitly encode multi-sensor data structures, mechanistic constraints, and probabilistic noise models [25, 26]. These approaches treat heterogeneous PAT channels as jointly informative measurements embedded within unified state-space or hybrid mechanistic–statistical formulations. For example, nonlinear state estimators such as EKF, UKF and moving-horizon observers have been applied to reconstruct solute concentration and crystal size distributions from multiple process measurements in seeded and industrial crystallization systems [27, 28]. In parallel, multi-PAT sensor arrays that combine spectroscopic and particle focused modalities have demonstrated the value of structurally modelling cross channel complementarity for polymorphism and particle size monitoring [29]. Nonetheless, these methods are often built upon assumptions of stable noise characteristics and consistently reliable sensor availability, whereas industrial crystallization environments exhibit dynamic hydrodynamics, varying solids loading and fluctuating PAT signal quality. Achieving robustness, physical consistency and interpretability simultaneously therefore remains a critical open challenge.

To address these challenges, a system level framework is developed that integrates multimodal PAT data simulation, dynamic sensor weight learning, and robust fusion. First, a multi-sensor data generation platform is established. This platform emulates industrial PAT behaviours with drift, offset, heteroscedastic noise, local dropouts and asynchronous sampling, aiming to generate complex and highly perturbed signals that capture the multi-factor variability observed under realistic industrial operating conditions. Next, an ML-based adaptive weighting mechanism is introduced to adjust sensor credibility in real time according to signal quality. Finally, robust statistical methods combined with temporal and physicochemical constraints ensure that the fused concentration and particle size trajectories remain smooth, consistent and physically coherent even under challenging noise conditions.

2. METHODOLOGY

2.1 PAT Data Structure and Feature Construction

The analysis considers four PAT channels: Raman and FTIR for concentration, and image-based sensors (IMA, e.g., PVM) and FBRM-proxy channels for particle size. Temperature is taken as the reference timeline, and all PAT streams are merged using an as-of alignment within a fixed tolerance so that each time point contains a consistent set of observations and associated time-step information. The aligned dataset is defined in **Eq. (1)**.

$$\mathcal{D}(t) = \{C_{\mathrm{Raman}}(t),\ C_{\mathrm{FTIR}}(t),\ L_{\mathrm{PVM}}(t),\ L_{\mathrm{FBRM}}(t),\ T(t)\} \quad (1)$$

Concentration-related feature vectors $X_{conc}(t)$ are formed from the instantaneous Raman and FTIR values, first-order temporal differences computed over a 7-point window, local variance estimates, normalised inter-channel discrepancies, and the time step statistics inherited from the alignment procedure. Spectral quality metadata including correlation coefficients and wavelength-shift indicators are included as direct numerical features when present in the raw PAT output.

Particle size feature vectors $X_{size}(t)$ comprise the instantaneous size estimates obtained from IMA, the calibrated FBRM-proxy signals, as well as derived descriptors including local temporal gradients, rolling-window variability, and the normalised discrepancy between the image-based and FBRM-proxy channels. To represent channel specific noise behaviour, image-quality indicators and count variance metrics associated with the construction of the FBRM-proxy are also incorporated.

For general applications, the underlying dataset must provide synchronised multi-sensor time series with explicit timestamps, channel resolved variance estimates, and relevant quality metadata. In the present study, all PAT datasets used for model development and evaluation are synthetically generated cases designed to strictly conform to this structural specification.

2.2 Pseudo-Label Construction and Model Training

For each case, Raman–FTIR and IMA–FBRM pairs are aligned on the common time axis. At each time index t, the two sensor readings $y_1(t)$ and $y_2(t)$, together with their nominal standard deviations $s_1(t)$ and $s_2(t)$, are combined to obtain a robust reference value. The reference is defined as the minimiser in **Eq. (2).**

$$x(t) = \arg\min_{x} \left[\rho\left(\frac{x - y_1(t)}{s_1(t)}\right) + \rho\left(\frac{x - y_2(t)}{s_2(t)}\right)\right] \quad (2)$$

where $\rho(\cdot)$ is the Huber loss. When only one measurement is available, the reference is taken directly from that channel. Residuals $r_i(t)$ are computed, and the normalised deviation is calculated in **Eq. (3)**, which is used to characterise the discrepancy between each sensor reading and the reference, relative to its nominal noise level. Based on this deviation, a variance inflation factor (VIF) (**Eq. (4)**) is assigned to each sensor and subsequently clipped within a fixed interval to suppress unrealistically large inflation values.

$$z_i(t) = \frac{|\, r_i(t)\,|}{s_i(t)} \tag{3}$$

$$\alpha_i(t) = \frac{r_i(t)^2}{s_i(t)^2} \tag{4}$$

A probability type failure indicator is constructed by combining $z_i(t)$ with channel specific quality metrics, including spectral correlation and peak-shift descriptors for Raman/FTIR, and image correlation and count-variance descriptors for IMA/FBRM. The final probability is obtained in **Eq. (5)**.

$$p_{\mathrm{bad},i}(t) = \sigma(z_i(t) + \gamma\, q_i(t)) \tag{5}$$

where $q_i(t)$ is the aggregated quality score and γ is a constant scale factor.

The input feature matrices are those constructed in Section 2.1. Two independent multi-output Random Forest regressors are trained for concentration and size separately. Each model outputs a four-dimensional vector ($p_{bad,\,i}(t)$, $\alpha_i(t)$). The regressors consist of 500 trees, use bootstrap sampling, employ mean-squared error as the splitting criterion, and restrict leaf size to a minimum of three samples to stabilise the estimates. Maximum tree depth is not constrained, allowing the ensemble to approximate nonlinear patterns. Feature subsets at each split are selected using sqrt-d sampling, where dis the number of feature dimensions.

The full dataset is randomly divided into an 80/20 train–test split with a fixed random seed to ensure reproducibility. Each Random Forest model is trained on the training portion and evaluated on the test portion using mean absolute error, root-mean-square deviation, coefficient of determination, and signed bias. After prediction, outputs corresponding to probability-type indicators are clipped to [0, 1], and VIFs are clipped to the prescribed interval. These trained regressors serve as the reliability estimators for the sensor weighting scheme used in the fusion procedure of Section 2.3.

2.3 Sensor Fusion with Constraints and Regularisation

The trained models provide estimates of the probability of sensor failure and the corresponding VIF. These outputs jointly modulate the effective contribution of each channel. A channel is considered unreliable when $p_{bad,\,i}(t)$ exceeds a high-risk threshold, in which case it is temporarily removed from fusion; when only one channel remains valid, the fused estimate simply follows that channel. For all remaining channels, the effective measurement uncertainty is computed in **Eq. (6)**. The precision score can be defined in **Eq. (7)**.

$$\tilde{v}_i(t) = \alpha_i(t)\, v_i(t) \tag{6}$$

$$\mathrm{prec}_i(t) = \frac{(1 - p_{\mathrm{bad},i}(t))^{\gamma}}{\tilde{v}_i(t)} \tag{7}$$

where γ controls the sharpness of the penalty applied to unreliable sensors. The contribution weights are then obtained by normalisation (Eq. (8)), after which they are smoothed in time to prevent abrupt switching caused by local noise or transient prediction variability. The fused estimate and its propagated variance follow the standard precision weighted averaging rules (**Eqs. (9-10)**).

$$w_i(t) = \frac{\mathrm{prec}_i(t)}{\sum_j \mathrm{prec}_j(t)} \tag{8}$$

$$y_{\mathrm{fused}}(t) = \sum_i w_i(t)\, y_i(t) \tag{9}$$

$$v_{\mathrm{fused}}(t) = \sum_i w_i^2(t)\, v_i(t) \tag{10}$$

Short gaps caused by sensor dropouts are filled by linear interpolation with aggressive variance inflation, ensuring that reconstructed segments carry low confidence and are naturally down weighted in later steps. To maintain consistency with crystallisation physics, the fused trajectories are further regularised by two physical constraints. The first ensures that the fused concentration remains consistent with the solubility relation at the corresponding temperature. The second enforces growth-dominated behaviour, where particle number is approximately conserved and the evolution of the characteristic size follows the prescribed baseline kinetics.

3. RESULTS AND DISCUSSION

3.1 Model Performance

The behaviour of each output in **Table 1** is consistent with the way pseudo-labels are generated in the training pipeline. In the code, both $p_{\mathrm{bad},i}(t)$ and $\alpha_i(t)$ are computed from residuals relative to a robust fused reference obtained via Huber IRLS. Channels whose simulated noise structure is tightly controlled (FBRM counts and IMA imaging) produce pseudo-labels with low intrinsic variability, resulting in smoother targets and correspondingly higher R^2 values for both p_{bad} and α. In contrast, the Raman and FTIR channels incorporate larger fluctuations in their synthetic noise terms, including peak-shift, correlation degradation and variable spectral perturbations. These lead to a wider spread in the pseudo-labels and therefore lower R^2 for the corresponding regression tasks.

For the probability type indicators $p_{\mathrm{bad},i}$, the mapping is dominated by monotonic functions of the normalised deviation $z_i(t)$ and channel specific quality metrics. These relationships are relatively smooth and piecewise monotonic, which aligns well with the structure of the RF

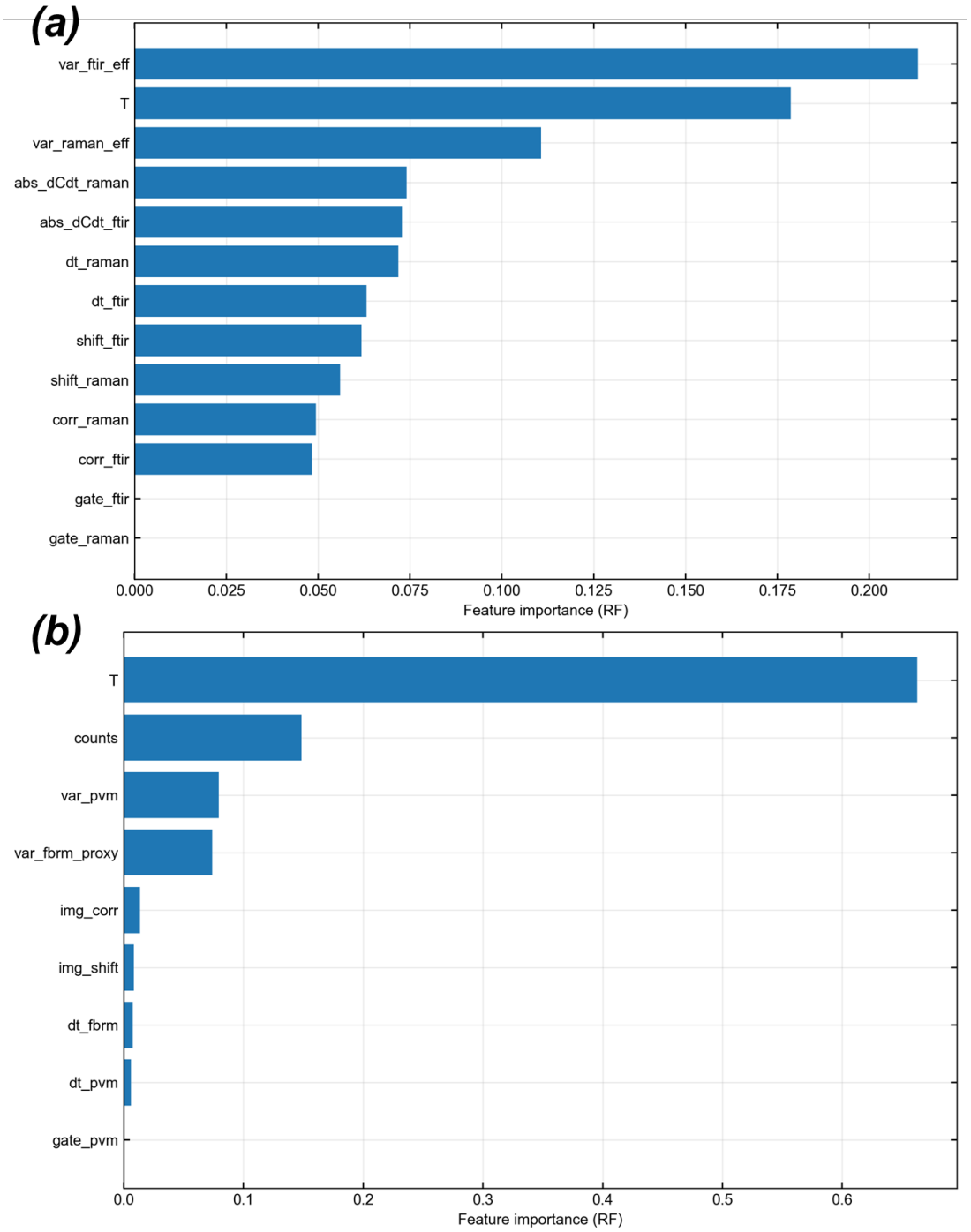

Figure 1. Feature importance of the RF models for (a) concentration and (b) particle size signals.

model. Consequently, all PAT channels yield low prediction errors and stable R^2, including the Raman and FTIR channels.

The VIFs $\alpha_i$depend quadratically on residuals, and therefore amplify local variability more strongly. In the synthetic dataset, the Raman and FTIR channels possess higher perturbation amplitude and more irregular local fluctuations. This produces labels with higher dispersion and less predictable fine-scale structure, reducing the achievable R^2even when MAE and bias remain small. The lower $R^2$for $\alpha_{\mathrm{Raman}}$and α_{FTIR}therefore reflects the variability present in the labels rather than a systematic model deficiency, and does not affect the downstream fusion

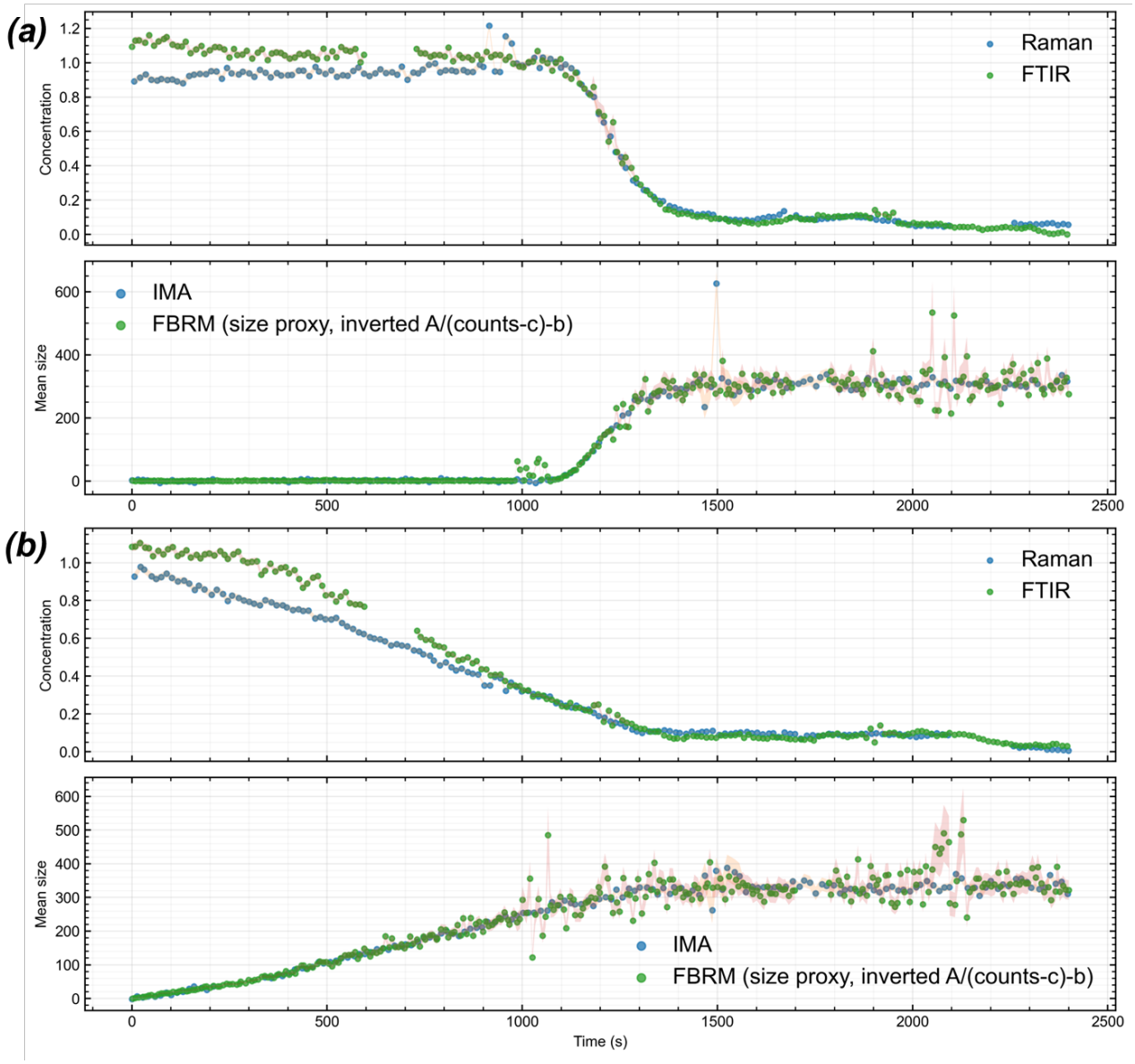

Figure 2. Synthetic scenarios used to evaluate fusion robustness cases (a) and (b).

stage where post clamped values are used only to modulate channel wise uncertainties.

Overall, the contrasting performance across channels directly follows from the pseudo label construction mechanism in the simulation code. The lower $R^2$for the Raman/FTIR αoutputs is expected under the imposed noise model and does not compromise the reliability estimates used in the subsequent fusion step.

The feature importance results reflect how the random forest allocates predictive weight across the input descriptors within the training dataset (**Figure 1**). For the concentration RF model, the highest ranked features are the effective variance terms (var_ftir_eff and var_raman_eff), followed by temperature and a set of short-term derivative descriptors (|dC/dt|, **Figure 1(a)**). These descriptors dominate the model's internal decision rules because they exhibit the strongest association with the pseudo-labelled reliability targets generated during training. Additional spectral structure descriptors, including peak-shift and correlation metrics, also receive non-negligible importance, consistent with their role in characterising signal perturbations within the dataset.

For the size RF model, temperature again appears with the highest importance values (**Figure 1(b)**). Other influential descriptors include the chord-count signal, variance terms derived from both IMA and FBRM-proxy channels, and image correlation and image shift measures. These variables receive higher weights

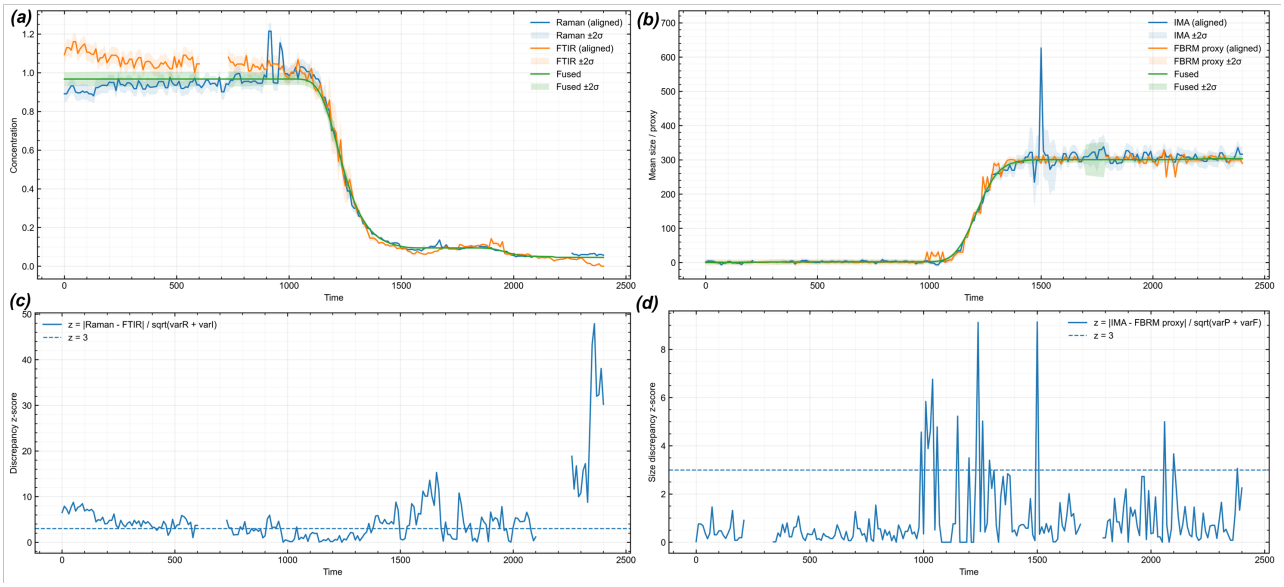

Figure 3. Multimodal PAT fusion results for Case 1. (**a**) aligned Raman and FTIR concentration measurements with fused estimates and uncertainty bands, (**b**) aligned IMA and FBRM-proxy mean size trajectories with fused estimates and uncertainty bands, and (**c–d**) discrepancy z-scores quantifying cross-sensor consistency over time.

because they co-vary with the reliability pseudo-labels across the synthetic cases used for training. Time-alignment and gating flags also contribute, although with lower importance relative to variance- and correlation-based descriptors.

Overall, the models emphasise descriptors that vary most consistently with the reliability pseudo-labels in the generated dataset, particularly those reflecting signal variance, short-term fluctuations, and structural perturbations in the PAT measurements. These importance patterns should be interpreted strictly as reflections of the models' internal learning behaviour under the specific data-generation and pseudo-labelling scheme adopted here, and do not imply generalisable diagnostic value beyond this study's design.

Table 1: Prediction performance of the multi-output Random Forest model for each PAT channel.

Output	MAE	RMSE	R^2	Bias
$P_{bad\ IMA}$	0.0605	0.1081	0.7220	-0.0041
α_{IMA}	0.7789	2.0620	0.8118	-0.0865
$P_{bad\ FBRM}$	0.0312	0.0586	0.9001	-0.0016
α_{FBRM}	0.2796	1.1892	0.9317	0.0017
$P_{bad\ Raman}$	0.1596	0.2115	0.5093	-0.0035
α_{Raman}	3.8445	5.6881	0.4896	-0.1377
$P_{bad\ FTIR}$	0.2047	0.2558	0.4654	0.0011
α_{FTIR}	6.1362	7.5885	0.4111	-0.0160

3.2 Case Studies

In this section two representative multimodal PAT cases are examined to illustrate the primary challenges in crystallization monitoring (**Figure 2**). Case a exhibits relatively stable concentration measurements but highly dynamic particle size evolution with an initial induction period, a rapid growth phase and sensor degradation episodes including imaging defocus, chord-length distortion and temporary dropouts. Case b features stronger baseline drift and temperature-dependent bias in the concentration channels, while the size measurements display continuous growth with local anomalies and inversion-related inconsistencies.

The fusion results for case 1 are available in **Figures 3 (a-d)**. The concentration trajectories in **Figure 3 (a)** show that Raman and FTIR follow the same overall evolution, although they display a noticeable baseline offset in the early stage. When the system enters the dominant crystallization transition between approximately 1100 and 1400 seconds, the two sensors respond coherently and the fused trajectory captures a physically smooth decline while presenting a narrower uncertainty envelope than either individual channel. This behaviour indicates effective fusion: the model is able to combine the complementary information from both sensors, reduce high-frequency noise and suppress misalignment-related variability. In the final segment of the experiment, roughly after 2200 seconds, the two concentration channels diverge substantially. The discrepancy z-score in **Figure 3 (c)** rises to values far beyond the expected statistical range, signalling that the disagreement between sensors is too large to be explained by their combined variance. This pattern is characteristic of sensor drift, intermittent artefacts or reliability degradation. The fused estimate remains stable during these periods and avoids

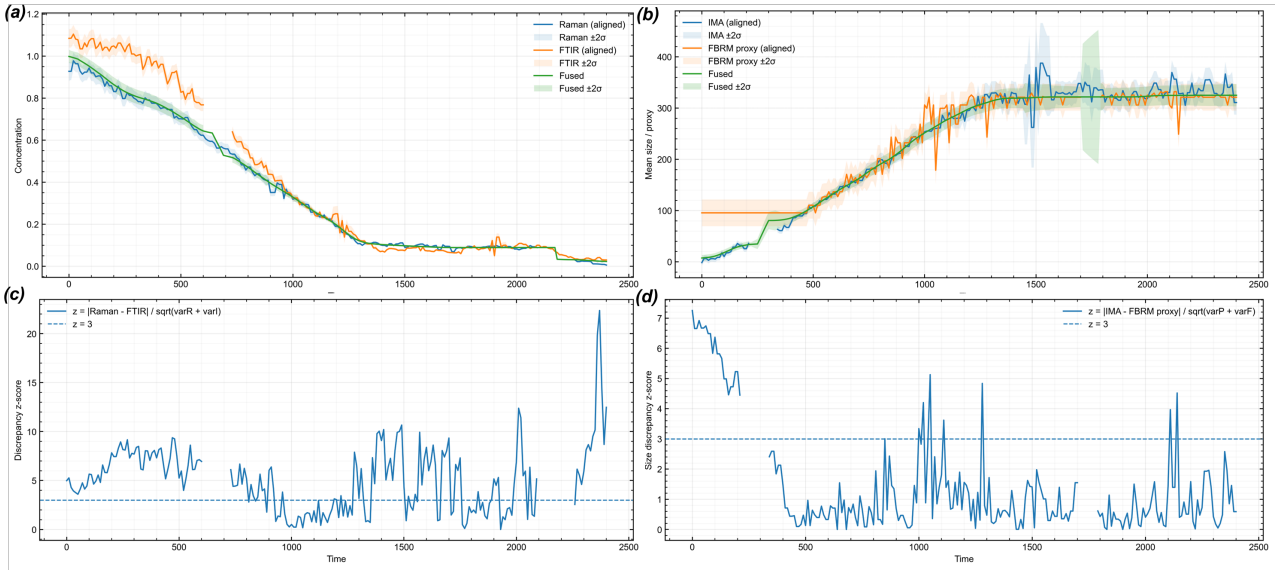

Figure 4. Multimodal PAT fusion results for Case 2. (**a**) aligned Raman and FTIR concentration measurements with fused estimates and uncertainty bands, (**b**) aligned IMA and FBRM-proxy mean size trajectories with fused estimates and uncertainty bands, and (**c–d**) discrepancy z-scores quantifying cross-sensor consistency over time.

propagating spurious fluctuations.

A similar behaviour is observed for the size signals in **Figure 3 (b)**. IMA and the FBRM-derived proxy exhibit consistent growth dynamics during the nucleation and growth regime and converge to a comparable plateau. IMA shows isolated spikes, most prominently near 1500 seconds. The fused estimate does not follow these irregular excursions and instead yields a smooth, monotonic trajectory that aligns with the expected crystallization trend. The discrepancy z-scores in **Figure 3 (d)** are small during the steady and slowly evolving periods, and markedly larger during transitional and disturbed regions. This indicates that the sensors agree well under stable conditions and that disagreements emerge mainly during rapid changes or localised noise events. Overall, the fused concentration and size trajectories are smoother, more physically interpretable and more robust to sensor artefacts than any individual signal.

In Case 2, the concentration signals display a stronger systematic discrepancy than in Case 1, with FTIR exhibiting an elevated baseline and larger drift throughout the early and mid stages (**Figures 4 (a-d)**). Despite the offset, both sensors follow similar downward kinetics, allowing the fused concentration to track the global trend while moderating channel specific bias and reducing local variance. The discrepancy z-scores remain consistently above the statistical threshold, indicating that the two sensors disagree more persistently than in Case 1 and signalling limited redundancy within the concentration pair.

For the particle size, IMA and the FBRM proxy show broadly similar growth behaviour during the early stage but diverge substantially after the main transition. IMA provides smoother and more continuous growth, while the FBRM proxy introduces abrupt fluctuations and intermittent artefacts, resulting in elevated size discrepancy z-scores across a wider time window. The fused size estimate mitigates these inconsistencies by suppressing FBRM-induced spikes and maintaining a physically coherent trajectory. Compared with Case 1, this case demonstrates higher cross-sensor disagreement and places greater emphasis on the fusion mechanism's ability to reject outliers and stabilise the evolution of both concentration and size.

3.3 Limitations and Future Perspectives

Although the present framework demonstrates robustness across heterogeneous PAT signals, several limitations remain. The analysis relies on synthetic scenarios and may not fully capture the complexity of real sensor behaviour, particularly long-term drift, chemometric model degradation, and process-dependent nonlinearities that can reshape the noise structure. In addition, the current fusion mechanism operates primarily at the signal level and does not explicitly integrate mechanistic constraints or population-balance consistency, which limits its ability to enforce global physical plausibility under severe sensor failure.

Future developments could incorporate hybrid physical statistical priors, adaptive drift modelling, and online reliability learning from historical process batches. Extending the framework to multivariate spectral domains, image-based morphological descriptors, and higher-frequency transient events would further enhance

its applicability to industrial crystallization.

4. CONCLUSIONS

This study developed a machine learning-assisted fusion framework for achieving reliable and physically coherent multimodal PAT monitoring in crystallization processes. By combining mechanistically informed data simulation, variance normalised discrepancy analysis and Random Forest-based reliability estimation, the method dynamically adjusts sensor contributions and mitigates the impact of drift, noise bursts, dropouts and cross-sensor inconsistencies. The physics-guided regularisation step further constrains the fused concentration and particle size trajectories to follow thermodynamic relations and growth-dominated crystallization behaviour.

Across two representative multimodal PAT scenarios, the framework consistently produced smoother, more interpretable and more robust trajectories than any individual sensor channel. In cases with mild disagreement, fusion effectively reduced noise and improved local consistency, whereas in scenarios with strong baseline drift or conflicting size measurements, the reliability model successfully down-weighted degraded sensors and preserved coherent kinetic trends. These results demonstrate that reliability-aware fusion can substantially enhance the integrity of multimodal crystallization monitoring under realistic industrial signal challenges.

ACKNOWLEDGEMENTS

This project has received funding under the call HORIZON-HLTH-2021-IND-07 (SusPharma, grant agreement no. 101057430) and under the UKRI Horizon Europe Guarantee scheme (SusPharma, project reference no. 10038378).

AUTHOR IDENTIFIERS

Author ORCIDs:
Yiming Ma: 0000-0001-6937-1924
Xuming Yuan: 0009-0006-2211-4879
Brahim Benyahia: 0000-0002-5397-1498

REFERENCES

1. Gao Y, Zhang T, Ma Y, Xue F, Gao Z, Hou B, Gong J. Application of pat-based feedback control approaches in pharmaceutical crystallization. Crystals 11:221 (2021). https://doi.org/10.3390/cryst11030221
2. Ma Y, Yuan X, Yewale A, Benyahia B. Recent advances in the digital transformation of crystallization process development and operation: synergy between model- and ai-driven strategies. Particuology 110:223-253 (2026). https://doi.org/10.1016/j.partic.2026.01.014
3. Ma Y, Wu S, Macaringue EGJ, Zhang T, Gong J, Wang J. Recent progress in continuous crystallization of pharmaceutical products: precise preparation and control. Org. Process Res. Dev. 24:1785-1801 (2020). https://doi.org/10.1021/acs.oprd.9b00362
4. Houson I, Siddique H, Chong MWS, Robertson M, Turner AJ, Nordon A, Osman A, Galindo A, Dunn AS, Johnston B, Benyahia B, Brown CJ, Mustoe CL, Price CJ, Reilly CD, Adjiman C, Jackson G, Prasad E, Halbert G, Feilden H, Sefcik J, McGinty J, Robertson J, Smith K, Al-Attili M, McGowan M, Siddique M, Pathan M, Rajoub N, Hamilton N, Feeney R, Brown S, Urwin SJ, Bernet T, Pickles T, Li W, Florence AJ. Quality by digital design in action: a workflow for crystallisation and isolation. International Journal of Pharmaceutics 686:126343 (2025). https://doi.org/10.1016/j.ijpharm.2025.126343
5. Li W, Hatcher LE, Wilson CC, Rielly CD, Benyahia B. A framework for systematic crystal shape tuning – case of lovastatin's needle-shaped crystals. Chemical Engineering Research and Design 202:126-146 (2024). https://doi.org/10.1016/j.cherd.2023.12.016
6. Houson I, Siddique H, Chong MWS, Robertson M, Turner AJ, Nordon A, Osman A, Galindo A, Dunn AS, Johnston B, Benyahia B, Brown CJ, Mustoe CL, Price CJ, Reilly CD, Adjiman C, Jackson G, Prasad E, Halbert G, Feilden H, Sefcik J, McGinty J, Robertson J, Smith K, Al-Attili M, McGowan M, Siddique M, Pathan M, Rajoub N, Hamilton N, Feeney R, Brown S, Urwin SJ, Bernet T, Pickles T, Li W, Florence AJ. Quality by digital design in action: a workflow for crystallisation and isolation. International Journal of Pharmaceutics 686:126343 (2025). https://doi.org/10.1016/j.ijpharm.2025.126343
7. Liu J, Benyahia B. Single and multiobjective shutdown optimization of a multistage continuous crystallizer. Ind. Eng. Chem. Res. : (2024). https://doi.org/10.1021/acs.iecr.3c03441
8. Yuan X, Nagy ZK, Benyahia B. A comprehensive framework for model evaluation and refinement using mbdoe estimability and structural identifiability: application to a crystallization process. Chemical Engineering Journal Advances 23:100823 (2025). https://doi.org/10.1016/j.ceja.2025.100823
9. Togkalidou T, Fujiwara M, Patel S, Braatz RD. Solute concentration prediction using chemometrics and ATR-FTIR spectroscopy. Journal of Crystal Growth 231:534-543 (2001).

https://doi.org/10.1016/s0022-0248(01)01518-4
10. Nagy ZK, Fujiwara M, Braatz RD. Monitoring and advanced control of crystallization processes. Handbook of Industrial Crystallization :313-345 (2019). https://doi.org/10.1017/9781139026949.011
11. Li W, Rielly CD, Benyahia B. Targeting desired particle size for improved dissolution and manufacturability of mefenamic acid. The 3rd International Online Conference on Crystals :21 (2022). https://doi.org/10.3390/iocc_2022-12165
12. Chong MWS, McGlone T, Chai CY, Briggs NEB, Brown CJ, Perciballi F, Dunn J, Parrott AJ, Dallin P, Andrews J, Nordon A, Florence AJ. Temperature correction of spectra to improve solute concentration monitoring by in situ ultraviolet and mid-infrared spectrometries toward isothermal local model performance. Org. Process Res. Dev. 26:3096-3105 (2022). https://doi.org/10.1021/acs.oprd.2c00238
13. Zhang F, Liu T, Wang XZ, Liu J, Jiang X. Comparative study on ATR-FTIR calibration models for monitoring solution concentration in cooling crystallization. Journal of Crystal Growth 459:50-55 (2017). https://doi.org/10.1016/j.jcrysgro.2016.11.064
14. Wynn EJW. Relationship between particle-size and chord-length distributions in focused beam reflectance measurement: stability of direct inversion and weighting. Powder Technology 133:125-133 (2003). https://doi.org/10.1016/s0032-5910(03)00084-6
15. Pandit AV, Ranade VV. Chord length distribution to particle size distribution. AIChE Journal 62:4215-4228 (2016). https://doi.org/10.1002/aic.15338
16. Cardona J, Ferreira C, McGinty J, Hamilton A, Agimelen OS, Cleary A, Atkinson R, Michie C, Marshall S, Chen YC, Sefcik J, Andonovic I, Tachtatzis C. Image analysis framework with focus evaluation for in situ characterisation of particle size and shape attributes. Chemical Engineering Science 191:208-231 (2018). https://doi.org/10.1016/j.ces.2018.06.067
17. Qu H, Alatalo H, Hatakka H, Kohonen J, Louhi-Kultanen M, Reinikainen SP, Kallas J. Raman and ATR FTIR spectroscopy in reactive crystallization: simultaneous monitoring of solute concentration and polymorphic state of the crystals. Journal of Crystal Growth 311:3466-3475 (2009). https://doi.org/10.1016/j.jcrysgro.2009.04.018
18. Zhao Y, Yuan J, Ji Z, Wang J, Rohani S. Combined application of in situ FBRM, ATR-FTIR, and raman on polymorphism transformation monitoring during the cooling crystallization. Ind. Eng. Chem. Res. :120912161452001 (2012). https://doi.org/10.1021/ie301241h
19. Orehek J, Tesli? D, Likozar B. Continuous crystallization processes in pharmaceutical manufacturing: a review. Org. Process Res. Dev. 25:16-42 (2020). https://doi.org/10.1021/acs.oprd.0c00398
20. Hansen TB, Simone E, Nagy Z, Qu H. Process analytical tools to control polymorphism and particle size in batch crystallization processes. Org. Process Res. Dev. 21:855-865 (2017). https://doi.org/10.1021/acs.oprd.7b00087
21. Zhao J, Wang M, Dong B, Feng Q, Xu C. Monitoring the polymorphic transformation of imidacloprid using in situ FBRM and PVM. Org. Process Res. Dev. 17:375-381 (2013). https://doi.org/10.1021/op300320a
22. Agimelen OS, Svoboda V, Ahmed B, Cardona J, Dziewierz J, Brown CJ, McGlone T, Cleary A, Tachtatzis C, Michie C, Florence AJ, Andonovic I, Mulholland AJ, Sefcik J. Multi-sensor inline measurements of crystal size and shape distributions during high shear wet milling of crystal slurries. Advanced Powder Technology 29:2987-2995 (2018). https://doi.org/10.1016/j.apt.2018.09.003
23. Fujiwara M, Chow PS, Ma DL, Braatz RD. Paracetamol crystallization using laser backscattering and ATR-FTIR spectroscopy: metastability, agglomeration, and control. Crystal Growth & Design 2:363-370 (2002). https://doi.org/10.1021/cg0200098
24. Trifkovic M, Sheikhzadeh M, Rohani S. Multivariable real?time optimal control of a cooling and antisolvent semibatch crystallization process. AIChE Journal 55:2591-2602 (2009). https://doi.org/10.1002/aic.11868
25. Wu WL, Mills MM, Schacht U, Rabinowitz C, Vlachos V, Nagy ZK. Sensor fusion and calibration-based adaptive image analysis procedure for in situ crystal size measurement. Crystal Growth & Design 23:7076-7089 (2023). https://doi.org/10.1021/acs.cgd.3c00273
26. Jul-Jørgensen I, Facco P, Gernaey KV, Barolo M, Hundahl CA. Data fusion of raman spectra in MSPC for fault detection and diagnosis in pharmaceutical manufacturing. Computers & Chemical Engineering 184:108647 (2024). https://doi.org/10.1016/j.compchemeng.2024.108647
27. Mesbah A, Huesman AEM, Kramer HJM, Van den Hof PMJ. A comparison of nonlinear observers for output feedback model-based control of seeded batch crystallization processes. Journal of Process Control 21:652-666 (2011). https://doi.org/10.1016/j.jprocont.2010.11.013
28. Porru M, Özkan L. Monitoring of batch industrial

crystallization with growth, nucleation, and agglomeration. part 2: structure design for state estimation with secondary measurements. Ind. Eng. Chem. Res. 56:9578-9592 (2017). https://doi.org/10.1021/acs.iecr.7b00243

29. Simone E, Saleemi AN, Nagy ZK. In situ monitoring of polymorphic transformations using a composite sensor array of raman, NIR, and atr-uv/vis spectroscopy, FBRM, and PVM for an intelligent decision support system. Org. Process Res. Dev. 19:167-177 (2014). https://doi.org/10.1021/op5000122